Shape of Multireference, Equation-of-Motion Coupled-Cluster, and Density Functional Theory Potential Energy Surfaces at a Conical Intersection

Samer Gozem,[†] Federico Melaccio,[‡] Alessio Valentini,[‡,§] Michael Filatov,[∥] Miquel Huix-Rotllant,[⊥] Nicolas Ferré,[⊥] Luis Manuel Frutos,[§] Celestino Angeli,[#] Anna I. Krylov,[▽] Alexander A. Granovsky,[○] Roland Lindh,[¶] and Massimo Olivucci*[,†,‡]

[†]Department of Chemistry, Bowling Green State University, Bowling Green, Ohio 43403, United States

[‡]Dipartimento di Biotecnologie, Chimica e Farmacia, Università di Siena, via A. Moro 2, I-53100 Siena, Italy

[§]Departamento de Química Física, Universidad de Alcalá, E-28871 Alcalá de Henares, Madrid, Spain

[∥]Institut für Physikalische und Theoretische Chemie, Universität Bonn, Beringstrasse 4, 53115 Bonn, Germany

[⊥]Aix-Marseille Université, CNRS, Institut de Chimie Radicalaire, Marseille, France

[#]Dipartimento di Scienze Chimiche e Farmaceutiche, Università di Ferrara, via Fossato di Mortara 17, I-44121 Ferrara, Italy

[▽]Department of Chemistry, University of Southern California, Los Angeles, California 90089-0482, United States

[○]Firefly Project, Moscow 117593, Russia

[¶]Department of Chemistry - Ångström, the Theoretical Chemistry Programme, POB 518, SE-751 20 Uppsala, Sweden

S *Supporting Information*

ABSTRACT: We report and characterize ground-state and excited-state potential energy profiles using a variety of electronic structure methods along a loop lying on the branching plane associated with a conical intersection (CI) of a reduced retinal model, the penta-2,4-dieniminium cation (PSB3). Whereas the performance of the equation-of-motion coupled-cluster, density functional theory, and multireference methods had been tested along the excited- and ground-state paths of PSB3 in our earlier work, the ability of these methods to correctly describe the potential energy surface shape along a CI branching plane has not yet been investigated. This is the focus of the present contribution. We find, in agreement with earlier studies by others, that standard time-dependent DFT (TDDFT) does not yield the correct two-dimensional (i.e., conical) crossing along the branching plane but rather a one-dimensional (i.e., linear) crossing along the same plane. The same type of behavior is found for SS-CASPT2(IPEA=0), SS-CASPT2(IPEA=0.25), spin-projected SF-TDDFT, EOM-SF-CCSD, and, finally, for the reference MRCISD+Q method. In contrast, we found that MRCISD, CASSCF, MS-CASPT2(IPEA=0), MS-CASPT2(IPEA=0.25), XMCQDPT2, QD-NEVPT2, non-spin-projected SF-TDDFT, and SI-SA-REKS yield the expected conical crossing. To assess the effect of the different crossing topologies (i.e., linear or conical) on the PSB3 photoisomerization efficiency, we discuss the results of 100 semiclassical trajectories computed by CASSCF and SS-CASPT2(IPEA=0.25) for a PSB3 derivative. We show that for the same initial conditions, the two methods yield similar dynamics leading to isomerization quantum yields that differ by only a few percent.
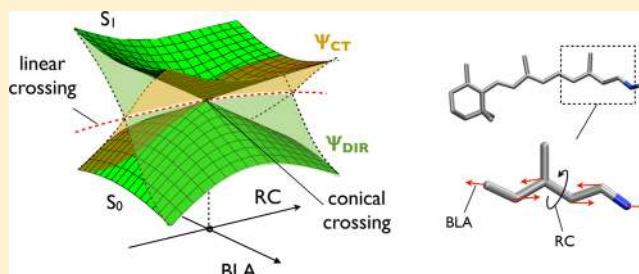
INTRODUCTION

A conical intersection (CI) is a specific molecular structure (a point in the space of nuclear configurations) where the potential energy surfaces corresponding to two electronic states of the same multiplicity cross[1,2] (here the "CI" label indicates a point of "conical intersection" and should not be confused with the configuration interaction method for which the CI acronym is commonly used). CIs are ubiquitous in polyatomic systems and play an important role in the photochemistry of organic,[3−8] inorganic,[9] and biological[10−12] systems. For example, the primary event in vision, the photoisomerization of the retinal

protonated Schiff base (rPSB) chromophore of visual pigments (see Scheme 1A), is mediated by a CI.[13−17]
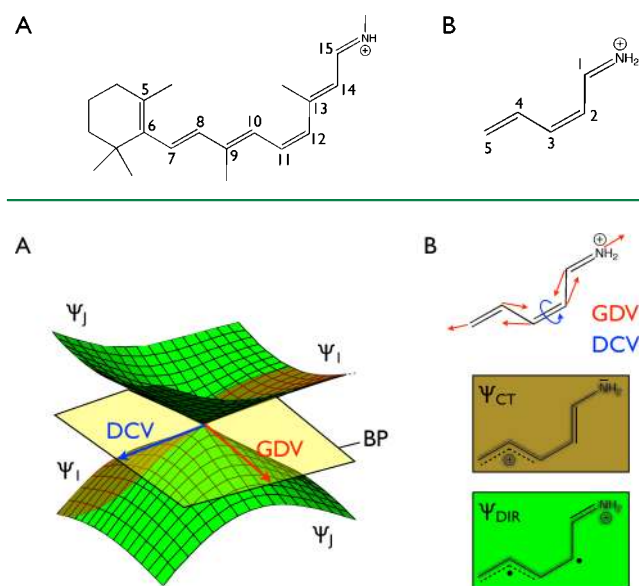
At a CI between two electronic states of the same spin and symmetry, the degeneracy can only be lifted by distorting the molecule along one of two specific degrees of freedom (see Figure 1A):

$$GDV_{IJ} = \frac{\partial}{\partial R}[E_I - E_J]$$

Scheme 1. Structure of rPSB (A) and Its Reduced Penta-2,4-dieniminium Cation Model (B)

Figure 1. (A) "Double-cone" representation of the potential energy surfaces of a molecular structure corresponding to a CI. The gradient difference vector (GDV) and the derivative coupling vector (DCV) that lift the energy degeneracy at a CI are shown as red and blue arrows, respectively. The two vectors define the branching plane (BP) shown in yellow. The surfaces in the panel are colored brown or green to distinguish regions of the potential energy surface dominated by different electronic configurations, represented by the adiabatic wave functions ψ_I or ψ_J. (B) Characteristics of penta-2,4-dieniminium cation (PSB3) at its minimum energy CI (information adapted from ref 29). On the top structure, the red and blue arrows indicate the GDV and DCV, respectively. The DCV corresponds to a torsional motion corresponding to the reaction coordinate (RC) driving the isomerization, and GDV is a bond length alternation coordinate corresponding to a lengthening of double bonds and shortening of single bonds along the backbone (BLA). The bottom two structures display bond-line diagrams of the two electronic configurations determining the character of the two states: one represents a charge-transfer electronic character, ψ_{CT}, and the other a diradical electronic character, ψ_{DIR}.

$$ \mathrm{DCV}_{IJ} = \left\langle \psi_I \left| \frac{\partial}{\partial R} \right| \psi_J \right\rangle $$

GDV denotes the gradient difference vector, DCV denotes the derivative coupling vector, E_I and E_J are the potential energies of the intersecting states, and ψ_I and ψ_J are the corresponding wave functions. These vectors are related to the **g** and **h** vectors that are commonly used to describe CIs.[18] GDV and **g** are identical, while DCV = $\mathbf{h}/(E_I - E_J)$ and is therefore parallel to **h**.[18] GDV and DCV define the so-called branching plane, also related to the **g**−**h** plane (Figure 1A). All degrees of freedom orthogonal to the BP vectors define a $3N - 8$ dimensional subspace called the intersection space (IS),[19] where N is the number of nuclei. Therefore, the IS forms a set of infinite CI points which, in general, have different structure and energy.

At a CI point, the excited and ground adiabatic states exchange their electronic characters. A molecule moving along the GDV on the upper state and passing to the lower state at the CI point preserves the character of its wave function, but the wave function of a molecule moving on the same adiabatic surface and passing through the CI would undergo a significant change (Figure 1A).

In order to locate and characterize the structure and properties of CIs, one needs appropriate computational tools that are able to deal with the following issues:

(1) The characterization and optimization of the CI[20−22] requires the GDV and DCV.[18] However, implementations of analytical DCVs are not always available in common quantum chemical packages, while, for sizable molecules, the evaluation of DCVs by finite differences is rather costly to be used within advanced electronic structure methods.

(2) Since a CI corresponds to a crossing of electronic states that may have very different electron distributions, appropriate electronic structure methods should provide a balanced description of both static and dynamic electron correlation. When a method fails to do so, the geometry of the crossing point may shift significantly, and its topography (e.g., peaked, intermediate or sloped)[19] may also change. However, appropriate methods are often computationally expensive.

(3) Not every method is capable of correctly describing the topology of the crossing along the BP, resulting in an incorrect dimensionality of the IS (the seam of CI points locally orthogonal to the BP).[19] (Here the term "topology" refers to the IS dimensionality and shall not be confused with the term "topography" which refers to the shape of the intersecting energy surfaces at a CI or "location" which refers to the geometry of the CI.)

Point 1 has been addressed by the development of approximate methods for obtaining the DCV,[23] or of algorithms for optimizing CI points without the need to compute the DCV.[24−28]

Point 2 is more difficult to address. We have recently presented a series of benchmark studies of the penta-2,4-dieniminium (PSB3) cation, a reduced model of rPSB (see Scheme 1B) exploring this issue. The reduced size of PSB3 allowed us to use high-level *ab initio* methods to compute the ground (S_0) and first excited (S_1) potential energy along pathways intercepting or running close to S_0/S_1 CI points[29,30] as well as to map a set of CI points belonging to the corresponding S_0/S_1 IS.[30] In PSB3, similar to rPSB, one of the states at the S_0/S_1 CI has a predominantly biradical electronic structure, ψ_{DIR}, and the other a predominantly charge-transfer character, ψ_{CT} (see Figure 1B).[29,31] By moving from one side of the CI to the other, the wave function changes its character if it remains on the same potential energy surface (e.g., such as ψ_I and ψ_J in Figure 1A).[19,32] The difference in the electronic structure of the two states near the CI makes it difficult to describe the surrounding region in PSB3: an unbalanced description of the two electronic states would cause their intersection to occur at a different geometry and even change the topography of the CI region[19] (as discussed in point 2 and already observed for PSB3 in ref 29).

The S_0 and S_1 pathways of PSB3 previously described were used to compare the accuracy of several methods with that of MRCISD+Q, taken as a reference. In particular, we tested different flavors of multireference perturbation theory (MR-PT2) approaches,[29,30] equation-of-motion coupled-cluster (EOM-CC) methods,[30,33] and density functional theory (DFT) based methods.[34,35] More recently, the same set of benchmarks was used by another group to test the spectroscopy oriented configuration interaction (SORCI) method.[36] These studies showed that both static and dynamic electron correlations are essential for a correct description of the region near the CI, requiring the use of quantitatively accurate and, therefore, expensive *ab initio* multireference or high-order EOM-CC methods. A natural temptation is to employ time-dependent DFT (TDDFT) to study CIs, which are inexpensive and yet provide a reasonable

description of excited states. This possibility has been discussed in the seminal work of Levine et al.[25] where it was shown that while standard TDDFT methods may be able to predict CI geometries quite accurately, they suffer from other problems. In particular, as we later explain, TDDFT methods cannot reproduce the correct IS *dimensionality* and, therefore, will not display a conical crossing in the BP.

This finally brings us to point number 3. As shown in Figure 1A, the energy degeneracy at a CI between the electronic states I and J may be split by one of two degrees of freedom, the GDV and the DCV. This property of CIs arises naturally when considering the secular eigenvalue equation for the two states of interest that have been decoupled from other states in a block Hamiltonian:

$$\begin{vmatrix} H_{II} - E & H_{IJ} \\ H_{JI} & H_{JJ} - E \end{vmatrix} = 0$$

where

$$H_{II} = \langle \psi_I | \hat{H} | \psi_I \rangle \qquad H_{IJ} = \langle \psi_I | \hat{H} | \psi_J \rangle$$

$$H_{JJ} = \langle \psi_J | \hat{H} | \psi_J \rangle \qquad H_{JI} = \langle \psi_J | \hat{H} | \psi_I \rangle$$

The solution of the preceding secular equation gives the energies of states I and J:

$$E_{I,J} = \frac{1}{2}\left[H_{II} + H_{JJ} \pm \sqrt{(H_{JJ} - H_{II})^2 + 4H_{IJ}H_{JI}} \right]$$

To satisfy the condition of degeneracy ($E_I = E_J$), the radicand must be equal to zero. Therefore, two independent conditions must be met: The off-diagonal coupling terms (H_{IJ} and H_{JI}, which are equivalent for a Hermitian operator $\hat{H}$) must vanish, and H_{II} and H_{JJ} must be equal. As demonstrated by Von Neumann and Wigner[37] and Teller,[1] meeting these conditions requires two independent nuclear coordinates. These are the GDV and DCV mentioned above, resulting in two-dimensional BP and an IS that spans a $(3N - 8)$-dimensional subspace.

These CI properties may be compromised when using approximate electronic structure methods that do not satisfy certain requirements. For instance, some methods cannot describe the electronic coupling between states I and J. For such methods, the off-diagonal coupling terms H_{IJ} and H_{JI} are always zero at any molecular geometry, and meeting the condition of energy degeneracy would only require one nuclear coordinate (for example, the GDV). As a result, for such methods the dimensionality of the IS increases from $3N - 8$ to $3N - 7$ and the local topology of the BP region surrounding a CI point changes (i.e., the crossing will not appear conical anymore but simply linear). As shown by Levine and Martinez,[14] this is the case for TDDFT, as well as for configuration interaction truncated at single excitations (CIS). A similar problem may be found in electronic structure methods that apply energy scaling corrections to H_{II} and H_{JJ} but that do not account for the effect of the scaling on the coupling between corresponding wave functions (in such cases, the intersection is displaced to another region of the potential energy surface but the electronic structures and couplings are not corrected, possibly leading to artifacts; e.g., see ref 29). For such approximate theories, it is no longer appropriate to refer to crossing points as "conical" intersections (e.g., as was done in refs 29, 30, and 33–35) as these are, topologically, "linear" intersections. This is also related to problem 1 since a method that does not split the degeneracy along DCV must resort to ways of optimizing a crossing point (which is not a true CI anymore) by using, for instance, the GDV

only.[24−27] To avoid confusion we also stress that crossing between states of different spin multiplicities are intrinsically "linear" (when using a nonrelativistic Hamiltonian) and that crossings between very weakly coupled states of the same spin multiplicity (such as in certain electron-transfer processes) may appear to be linear but they are not.

The dimensionality of the IS also depends on the hermiticity of the Hamiltonian operator. In theories that employ a non-hermitian "effective" Hamiltonian (i.e., theories leading to nonsymmetric effective Hamiltonians), the condition of energy degeneracy is only met if three conditions are satisfied: H_{IJ} and H_{JI} must be equal, and they must both be zero, and H_{II} and H_{JJ} must be equal to each other as well. In this case, *three* independent nuclear coordinates are required, and the IS spans $3N - 9$ dimensions. For such nonhermitian theories (coupled-cluster methods fall in this category), the topology of the region surrounding the CI is incorrect and the crossing is not conical, having a three-dimensional BP. This is explained nicely in refs 38 and 39.

While the above theoretical considerations are important, it is not always straightforward to determine, *a priori*, if a method would successfully describe the correct CI topology, especially with modern methods that have sometimes very complex formalisms. To address this point, we extend our previous benchmark studies[29,30] to the current one where we directly probe the dimensionality of the BP surrounding a CI. In one of these earlier studies,[29] we mapped several pathways on the S_0 surface near the CI for PSB3 at the CASSCF level of theory (see Figure 2A for a schematic representation of the CASSCF S_0 surface of PSB3 in the CI region). One of the paths follows the BLA coordinate (yellow cross-section in Figure 2A,B) introduced in the legend of Figure 1 and measured as the difference between the average value of the single-bond lengths and the average value of the double-bond lengths in the back-bone of PSB3. This is mostly parallel to the GDV in PSB3 (see Figure 1B, top). Other pathways correspond to minimum energy paths that follow a torsion coordinate roughly parallel to the DCV (again, see Figure 1B, top). Finally, in the same study, we also constructed a small (milliangstrom) loop around the CI employing CASSCF computed GDV and DCV vectors (see blue circular cross-section in Figure 2A,C). The corresponding S_0 and S_1 energies were then computed along the loop (see Figure 2D). Since the loop incorporates a CI point and lies on BP, we would expect that (i) S_0 and S_1 are not degenerate at any point along the loop, because the GDV and DCV split the degeneracy and the crossing has a conical shape; and (ii) the S_0 and S_1 wave functions along such a loop change electronic character twice, once from ψ_{CT} to ψ_{DIR} and once from ψ_{DIR} to ψ_{CT}. As reported in Figure 2D, this is indeed what was observed in ref 29. However, when more accurate electronic structure methods were employed, it was found that the crossing point (corresponding to the CI determined at the CASSCF level) had shifted location along the BLA coordinate and ended up outside the loop. Therefore, while the previous PSB3 studies partially addressed the issue of testing the shape of the crossing, a more rigorous testing of all of the methods was not performed. In this study, we employ PSB3 again as a model to test the shape (topography) and dimensionality (topology) of the crossing along BP for each class of methods. To this end, we construct several loops centered at a crossing point corresponding to each of these methods and use them to scan the energy around the crossing. Such a test provides a quick way to distinguish between methods that produce conical crossings (with $(3N - 8)$-dimensional IS) from those that produce linear crossings ($(3N - 7)$-dimensional IS). Note that,
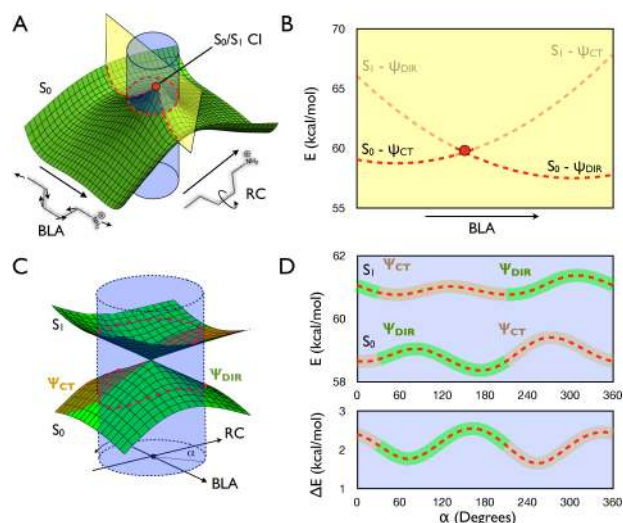
Figure 2. (A) Schematic representation of the PSB3 S_0 potential energy surface in the region of a S_0/S_1 CI and along a two-dimensional space defined by BLA and RC (defined in Figure 1B) that roughly correspond to BP. The BLA coordinate and the CI loop cross-sections from ref 29 are shown in yellow and blue, respectively. (B) The S_0 (opaque) and S_1 (translucent) CASSCF energy profiles along the BLA coordinate. (C) More detailed scheme of the CI loop scan. Both the S_0 and S_1 surfaces are shown. The loop is at the intersection of the circumference of the blue cylinder with the S_0 and S_1 potential energy surfaces (shown as red dashed lines) and lies in the branching plane defined by RC and BLA, assumed to be parallel to the DCV and GDV, respectively. Along the loop, the wave function of each state is expected to change electronic character twice. Areas of the surface shaded brown have a predominantly charge-transfer wave function, ψ_{CT}, while green regions have a predominately diradical wave function, ψ_{DIR}. (D) S_0 and S_1 CASSCF energies (top) and S_0-S_1 energy gap (bottom) along the CI loop as a function of α (as labeled in panel C). The energy profiles are shaded green or brown to show the dominant electronic character of the wave function for each state at that point (for the energy gap, only the character of the S_0 wave function is shown).

since the BP is assumed to be two-dimensional, this test can only distinguish between CI points belonging to a $\leq(3N-8)$-dimensional from those belonging to a $(3N-7)$-dimensional IS. Therefore, it cannot distinguish between methods that produce a $3N-9$ IS from those that have the correct $(3N-8)$-dimensional IS. The latter distinction is usually easier to recognize from theory (it arises whenever a nonhermitian effective Hamiltonian is used). In the final section, we test the effect of the shape of the surface near a crossing by running a set of 100 semiclassical trajectories using a PSB3 derivative with a substitution pattern resembling that of the all-*trans*-rPSB chromophore of microbial rhodopsins. In particular, we run the same set of 100 trajectories at two levels of theory, one which has a correct (conical) crossing shape and one corresponding to a linear crossing. Details regarding the computations are provided in the next section.

■ METHODS

We test three different flavors of MR-PT2 (CASPT2,[40] XMCQDPT2,[41] and QD-NEVPT2[42,43]), one variant of spin-flip EOM-CC[44−47] (EOM-SF-CCSD(dT)[48]), and three different flavors of DFT (TDDFT with the mPW2PLYP functional,[49−51] SI-SA-REKS with the HF and BH&HLYP functionals,[52] and a collinear formulation of SF-TDDFT[53] with the BH&HLYP[52] functional). All TDDFT calculations employed the Tamm−Dancoff approximation.

All calculations were performed with the 6-31G* basis set consistently with earlier benchmark studies on PSB3.[29,30,33−35] In the following section, we first present details about the construction of the loops. Then, we present computational details regarding the tested methods.

**Construction of Loops Centered at Crossing Points.** The loops were all consistently centered at the crossing points located along the BLA scan from refs 29, 33, and 35 and reported in the top of Figure 3 (see loops A−D in Figure 3). Since some methods yielded crossing points at larger BLA values (i.e., outside the BLA scan in refs 29, 33, and 35), for these methods we computed the energy profiles along an extended region of the BLA, located their S_0/S_1 crossing points, and constructed separate loops for each crossing as well (loops E and F in Figure 4). In particular, loop A is centered at the CASSCF crossing (this is the same loop presented in ref 29 and in Figure 2D), loop B is centered at the SS-CASPT2(IPEA=0) crossing, loop C is centered at the MRCISD crossing, loop D is centered at the MRCISD+Q crossing, loop E is centered at the SI-SA-REKS/BH&HLYP crossing, and loop F is centered at the SF-TDDFT crossing. Other methods have similar crossing points as MRCISD+Q or CASSCF, so we do not construct separate loops for all of them but rather employ loops A and D to test them. The geometries of the crossing points around which the loops are centered are shown in Figure S1 of the Supporting Information (SI). All loops have a radius of 0.002 Å and lie along the BP vectors computed at the CASSCF level of theory. Loops with small radii were used in order to capture the exact shape of the potential energy surfaces at the crossing. We assume that the CASSCF vectors are transferable to other crossing points or that they have a large projection on BP vectors that would have been computed at a different level of theory. As also discussed in the literature,[4,54] this assumption is physically grounded. In fact, the BP vectors must correspond to torsional mode (ca. RC) that most rapidly allows for the reconstitution of the π-overlap across the central orthogonally twisted double bond and a stretching mode (ca. BLA) which induces the charge transfer along the π-framework by effectively changing the pairing between all π-electrons. The BP vectors computed at different levels of theory shall thus be similar to the CASSCF ones. For comparison, the SI-SA-REKS BP vectors were also computed and compared to those of CASSCF in Figure S2 of the SI, indeed they were found to be similar.

Multiconfigurational Methods. CASSCF and MR-PT2 calculations (with the exception of QD-NEVPT2) employ an active space of six electrons in six π-orbitals involving the bonding and antibonding orbitals related to the π-conjugated system in PSB3. For CASPT2, we test both single-state (SS) and multistate (MS)[55] variants of CASPT2, both with and without the default IPEA parameter.[56] All SS-CASPT2 and MS-CASPT2 energies were obtained with an imaginary shift of 0.2 to exclude intruder states. Similarly, in XMCQDPT2, an intruder state avoidance (ISA) shift of 0.02 was used. In this work, all reported XMCQDPT2 energies are computed with a modified Fock-like operator which incorporates some terms arising from the nonseparable part (Γ_{ns}) of the CASSCF state-averaged second-order density matrix, Γ. This version of XMCQDPT2 is used because it appears to better reproduce MRCISD+Q energy profiles in PSB3 and because it yields a crossing geometry similar to that of MRCISD+Q.[29,30] QD-NEVPT2 energies are computed with the partially contracted variant and employed a larger active space of six electrons in eight orbitals (including two additional virtual π^*-orbitals) because that was found to improve the agreement with MRCISD+Q.[29] Finally, MRCISD calculations
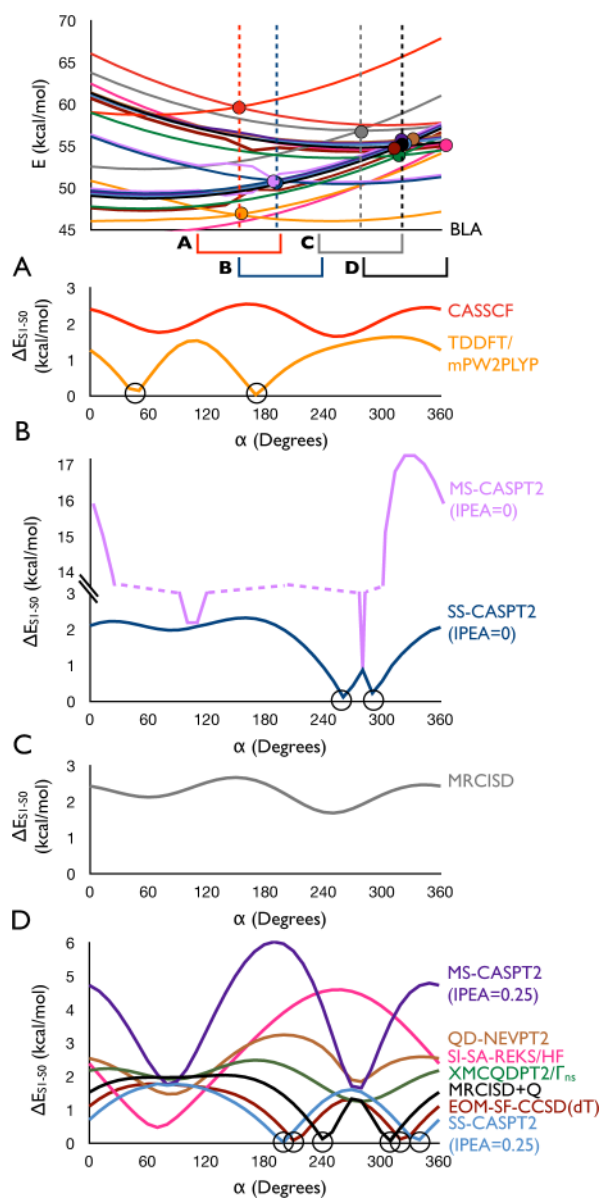
Figure 3. BLA and CI loop energy profiles for CASSCF (red, same as Figure 2D, bottom), MRCISD (gray), MRCISD+Q (black), SS-CASPT2(IPEA=0) (dark blue), MS-CASPT2(IPEA=0) (violet), SS-CASPT2(IPEA=0.25) (light blue), MS-CASPT2(IPEA=0.25) (violet), XMCQDPT2/Γ_{ns} (green), QD-NEVPT2 (brown), TDDFT/mPW2PLYP (orange), and SI-SA-REKS-HF (fuchsia). (Top) S_0 and S_1 energy profiles along the BLA scan, relative to cis-PSB3. The positions of the crossings are shown as filled circles. Due to the different geometries of the crossings at different levels of theory, several CI loops were constructed, each centered at a different BLA value, to incorporate the crossings of all tested methods. One loop was centered at the CASSCF crossing (panel A), one around the MRCISD crossing (panel B), one around the CASPT2(IPEA=0) crossing (panel C), and one around the MRCISD+Q crossing (panel D). Note that MRCISD+Q, SS-CASPT2-(IPEA=0.25), MS-CASPT2 (IPEA=0.25), XMCQDPT2, QD-NEVPT2, EOM-SF-CCSD(dT), and SI-SA-REKS all have similar energy profiles along the BLA and a similar geometry for the crossing, and therefore only one loop is used to test all seven methods. Along the loops, only the energy differences between S_0 and S_1 are shown for all methods. An energy difference of ~0 kcal/mol means that the two states cross at that point. Such crossing points are indicated by black circles.

employed the same six electron six orbitals reference active space as in CASSCF. The internally contracted version of MRCISD
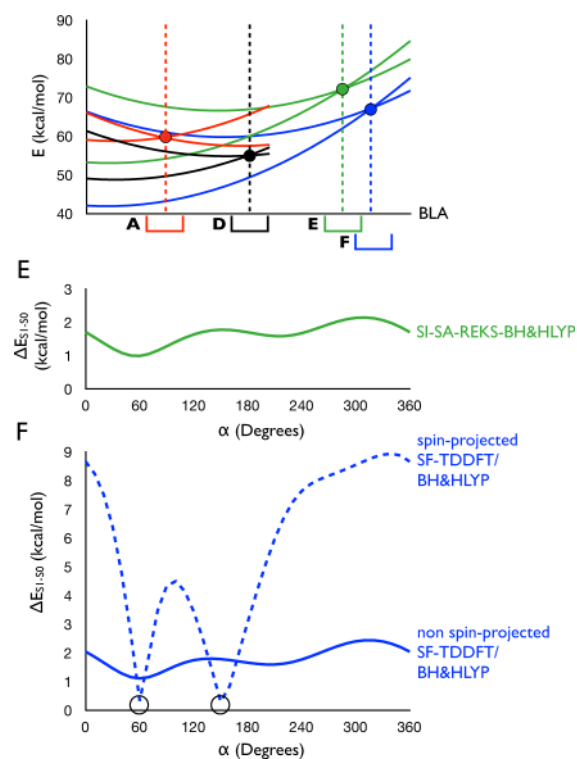
Figure 4. (Top) S_0 and S_1 energy profiles along a more extended region of the BLA scan, relative to cis-PSB3. The BLA energy profiles are shown for CASSCF (red), MRCISD+Q (black), SI-SA-REKS/BH&HLYP (green), and SF-TDDFT/BH&HLYP without spin projection. The CASSCF and MRCISD+Q profiles are shown to allow comparison of the scale with Figure 3. The positions of the conical intersections are shown as filled circles at the different levels of theory. Panel E displays SI-SA-REKS/BH&HLYP energy profile centered at its corresponding crossing point. Panel F displays the SF-TDDFT/BH&HLYP energy profile both with spin projection (dashed lines) and without (solid lines) around a loop centered on the SF-TDDFT/BH&HLYP crossing found without spin projection. Along the loops, only the energy differences between S_0 and S_1 are shown for all methods. An energy difference of ~0 kcal/mol means that the two states cross at that point. Such crossing points are indicated by black circles.

was used, and for MRCISD+Q the Davidson correction[57] with a relaxed reference[58] was employed. Core orbitals in all MR-PT2 and MRCI calculations were frozen.

EOM-CC Methods. Only EOM-SF-CCSD(dT) was tested owing to its success in previous benchmarks.[29,30] This version of EOM-CC employs the spin-flip operator,[44−47] with a ROHF triplet reference state (ROHF is used to reduce spin contamination). The triples correction (dT) is derived by using second-order Rayleigh−Schrödinger perturbation theory starting from the EOM-SF-CCSD solutions as zero-order states[48] and employing the diagonal of the full similarity transformed Hamiltonian. All electrons were correlated in the CCSD and EOM calculations.

Density Functional Theory Methods. Three types of DFT methods were tested. The first is a linear response TDDFT approach with a double-hybrid mPW2PLYP functional[49−51] and using the Tamm−Dancoff approximation.[59] The mPW2PLYP functional was chosen because it did not have severe self-consistent field (SCF) convergence issues near the crossing geometry, where the other density functionals tested in ref 35 did experience serious convergence difficulties. However, for the purpose of this work it is also a representative method that is expected to behave like any other DFT functional within

TDDFT. The second method is REKS, an ensemble DFT method whose formulation is described in ref 60. While REKS is a ground-state method, excited states can be accessed by using state-averaged REKS (SA-REKS).[61] In particular, we also use a state-interaction SI-SA-REKS approach introduced in refs 35 and 62. We test REKS with two different functionals, which are the HF and BH&HLYP functionals, as used in refs 35 and 62. Note that the idea of state interaction has recently been used by Li et al.[63] in the context of TDDFT. This method, the configuration interaction corrected Tamm–Dancoff approximation (CIC-TDA) DFT, is not tested in the present work; it has already been shown to yield the correct dimensionality of the BP. Finally, the third DFT method tested is the spin-flip TDDFT (SF-TDDFT)[53,64] method (the original collinear variant) employing the BH&HLYP functional.[52] We test SF-TDDFT in its original, non-spin-adapted, implementation,[53] which may lead to spin contamination in the target states, as well as a spin-projected variant.[65,66]

CASSCF and CASPT2 Semiclassical Trajectories. In order to understand the effects of the BP shape on semiclassical dynamics, we computed a series of surface hopping molecular dynamics trajectories using a set of 100 sampled initial conditions. These 100 initial structures and velocities were prepared by thermal sampling according to the Boltzmann distribution at room temperature and at the HF level of theory (which is qualitatively correct around the equilibrium geometry). The initial conditions were generated by quasi-classical fixed local mode sampling at 298 K and 1 atm, as implemented in Gaussian (and based on VENUS96[67]). These structures and velocities were then used as starting points to launch trajectory calculations using the Dynamix module in Molcas[68] (for more details on Dynamix see ref 69). Briefly, the trajectories were propagated using Newton's equations of motion and according to the velocity Verlet algorithm[70] with a time step of 1 fs.

The surface hopping events (i.e., nonadiabatic transitions) were imposed using Tully's fewest switches algorithm.[71] The electronic states of the system were described by CASSCF or SS-CASPT2 wave functions with a total of six electrons in six orbitals defining the complete π-system. In order to determine the time-dependent wave function and the population of each electronic state with time, a set of 200 substeps of integrations (5×10^{-3} fs) of the time-dependent Schrödinger equation were performed for each Newton equation-of-motion integration step (1 fs). The projection of the DCV along the trajectory was computed by finite differences at each step of the nuclear motion integration following an equivalent scheme as in ref 15; i.e., the derivative of the wave function is taken as a finite variation between two consecutive configuration interaction vectors of the trajectory. In order to determine the derivative coupling elements for each electronic-integration substep, an interpolation–extrapolation scheme was used.[72] Finally, the decoherence correction due to Granucci and Persico is employed to improve the internal consistency of the surface hopping algorithm.[73]

Software Used. Calculations were performed in Gaussian 03[74] (for CASSCF energies, BP vectors, and thermal sampling of initial conditions), Molcas 7.8[68] (for the CASSCF and CASPT2 energies and trajectory calculations), Molpro[75] (for the MRCISD and MRCISD+Q energies), Gamess-US[76] (for SF-TDDFT calculations), Firefly[27] (for the XMCQDPT2 energies), Q-Chem[77] (for EOM-SF-CCSD(dT) energies), Orca[78] (for the TDDFT energies), and COLOGNE2012[79] (for the REKS BP vectors and energies). QD-NEVPT2 calculations have been performed using a code developed at the University of

Ferrara and interfaced to Molcas. Loops were constructed using MOplot v. 1.86.[80]

■ RESULTS AND DISCUSSION

CI Loop Scan Results. In Figures 3 and 4, we present the S_0–S_1 energy gaps along loops centered at a crossing point for each electronic structure method. For better readability, we present the energy gap rather than S_0–S_1 energies (similar to Figure 2D bottom). The corresponding S_0 and S_1 energy profiles are provided in Figures S3–S16 the SI. In all cases, we confirmed that the crossing for each level of theory lies inside the respective loop for which the energy profile was computed by either checking the electronic character for a single state along the loop (i.e., that it changes twice passing from a dominant ψ_{CT} to a dominant ψ_{DIR} and vice versa) or by checking that the uncoupled ("diabatic") states cross twice along the loop for each method (see SI Figures S3–S16) by monitoring the change in wave function character. The results show the following:

(a) CASSCF, as discussed previously, behaves correctly and the corresponding CASSCF crossing is conical, that is, a real CI (see Figure 3A). The energies of the S_1 and the S_0 states never cross so that their energy difference is always larger than zero and displays two maxima and two minima.

(b) MRCISD also behaves correctly for a real CI (Figure 3C), as already demonstrated,[81] but when the Davidson correction is applied, the states intersect twice along the loop (Figure 3D) as shown by the state energy difference which goes twice to zero. This is due to the fact that the Davidson correction only corrects the energies but does not correct the couplings. Therefore, MRCISD+Q does not produce a conical crossing but rather a linear crossing within the BP. Accordingly, at this level of theory we expect a $(3N - 7)$-dimensional IS.

(c) SS-CASPT2 does not account for any coupling between the two states and therefore displays two points where the energy gap is zero (i.e., where S_0 and S_1 cross), as shown in Figure 3B for CASPT2 without the IPEA shift. This behavior of SS-CASPT2 has been first documented by Malrieu et al.,[82] where it was shown that SS-CASPT2 displayed a double crossing along the Li–F stretching coordinate rather than an avoided crossing. This work led to the development of the MS-CASPT2 formalism[55] that is based on a multipartitioning approach,[83] where a separate zero-order Hamiltonian is used for each state. MS-CASPT2, through the multistate Hamiltonian, couples the two states, and they no longer cross. For example, MS-CASPT2 has been shown to yield the correct dimensionality of the BP and IS in refs 25 and 84. However, it is also important to notice the large difference in energy profiles between SS-CASPT2 and MS-CASPT2 in Figure 3B. This is due to a previously documented behavior. In particular, we find that MS-CASPT2 tends to drastically over-estimate the coupling between the two intersecting states.[29,41] This is clearly demonstrated since the MS-CASPT2 energy gap oscillates between <1 and 17 kcal/mol (compared to a maximum energy gap of ca. 3 kcal/mol with other methods). This implies that, unrealistically, in the case of MS-CASPT2 the CI appears to lie in a very steep valley surrounded by high barriers on two sides. Note that these artifacts in MS-CASPT2 can be corrected by applying an extension similar to that used in XMCQDPT2, as demonstrated in ref 85. Finally, the MS-CASPT2 Hamiltonian matrix is generally nonsymmetric, and would produce a CI with a (3N-9)-dimensional IS. Symmetrization of the MS-CASPT2 Hamiltonian is needed to produce the correct (3N-8)-dimensional IS. On the other hand, instead of symmetrization one may be able to ensure that H_{IJ} and H_{JI} are

similar by, for instance, increasing the active space used in the calculation.[86]

(d) SS-CASPT2 and MS-CASPT2 with IPEA = 0.25 behave similarly to those without IPEA (see Figure 3D). Therefore, S_0 and S_1 cross twice at the SS-CASPT2 level but do not cross in the case of MS-CASPT2. Again, we see an overestimation of the coupling in MS-CASPT2 but not as severe as in Figure 3B. This may simply be due to the use of the CASSCF BP vectors, which are naturally more accurate at the CASSCF crossing rather than at the MS-CASPT2 crossing.

(e) XMCQDPT2 and QD-NEVPT2 both behave correctly along the loop (Figure 3D) and therefore identify real CI points. This is due to the diagonalization of the multistate Hamiltonians. In fact, as expected, when plotting just the diagonal elements of the Hamiltonian we see that the underlying "diabatic" states cross twice along the loop (see SI Figures S8 and S9). As in MS-CASPT2, the QD-NEVPT2 Hamiltonian matrix must be symmetrized to produce the $(3N − 8)$- rather than $(3N − 9)$-dimensional IS.

(f) EOM-SF-CCSD(dT) behaves similarly to MRCISD+Q and SS-CASPT2, we observe that the states cross twice along the loop (Figure 3D). Due to the nonhermiticity of the EOM-CC theory, we expect that EOM-CC methods would produce a CI that occupies a $(3N − 9)$-dimensional IS.[38,39] However, the results of the loop scan indicates a linear crossing, which suggests that the IS is $(3N − 7)$-dimensional. This is likely due to the perturbative (dT) correction, which uses EOM-SF-CCSD as a reference and corrects the energy to account for triple excitations. The limitations of such an approach are the same as of the Davidson correction discussed above.

(g) The states computed with TDDFT/mPW2PLYP display two crossing points along the loop in Figure 3A, as anticipated earlier.[14]

(h) The SI-SA-REKS states are allowed to couple through the application of the state interaction (Figures 3D and 4E), and therefore SI-SA-REKS displays the correct conical dimensionality of the crossing, as also shown in a recent study.[62] This behavior should be independent of the functional used (HF or BH&HLYP). In Figure 3D, SI-SA-REKS-HF displays a different energy profile along the loop with respect to other methods, but this is likely due to the fact the SI-SA-REKS-HF crossing does not lie at the center of the loop from Figure 3D that was centered on the MRCISD+Q crossing. Indeed, the loop in Figure 4E, which is centered on the SI-SA-REKS/BH&HLYP, displays a profile very consistent with other methods.

(i) In the case of spin-projected SF-TDDFT we find that the states do cross along the loop. However, non-spin-projected SF-TDDFT displays the correct dimensionality of the BP (see Figure 4F), as expected for a CIS-type approach in the case of CIs between two target states (rather than a reference and an excited state).[87] Note that the crossing of the SF-TDDFT states occurs at a large BLA value. This is because the minimum energy CI (MECI) computed with SF-TDDFT using the approach of Maeda et al.[23] is slightly pyramidalized at one of the double-bond carbons (see Figure S17 in the SI, where we compare the geometry of the SF-TDDFT MECI with those of SI-SA-REKS/BH&HLYP and MS-CASPT2[88]) possibly indicating problems in describing diradicals. However, to be fully consistent with the way all other methods were tested, here we use the crossing obtained along the BLA scan rather than the MECI crossing. More accurate state energies and therefore crossing positions may be obtained with different functionals,

as found in refs 34 and 89. Note that SF-TDDFT has already been demonstrated to split the degeneracy at the CI in ethylene by Minezawa and Gordon.[90] It also has yielded a correct shape of the potential energy surface around the CI mediating the photochemical ring opening of oxirane.[91] Here we confirm these results by using a loop centered at a CI point. However, in both of these cases, spin projection was not performed. By applying Yamaguchi's approximate spin-projection formula,[65,66] the correct dimensionality of the BP is lost. Thus, if spin adaptation is desired, one should proceed by creating a spin-complete set of determinants, as was done within the configuration interaction formalism[92] and discussed by Rinkevicius et al. in the context of SF-TDDFT.[93]

Branching Plane Scans. In order to further verify the results from Figures 3 and 4, a plot in the plane of the BP was produced for some selected methods (see Figure 5). The results in these plots reflect what was already demonstrated in Figures 3 and 4. First, we find that the CASSCF CI is peaked and displays the correct branching plane conical topology. In contrast, SS-CASPT2 with IPEA = 0.25 clearly displays a linear rather than
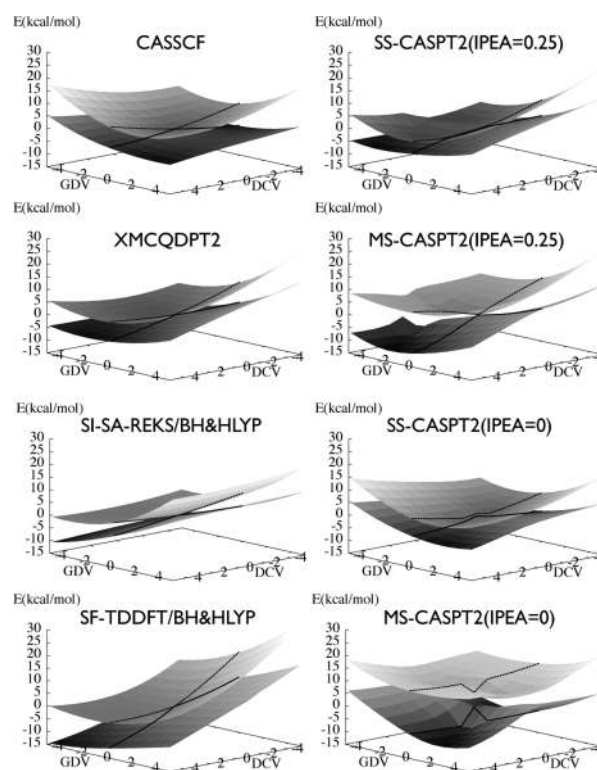

Figure 5. S_0 and S_1 energy profiles along a 2D scan scanning the branching plane. These plots were produced by changing the CI structure along the GDV and DCV to produce an 11×11 grid of points centered at the CI. The vectors used were the CASSCF ones (with the exception of DFT methods, for which the vectors were obtained at the respective level of theory), and were first normalized to 1 Å using the spectral matrix norm. The normalized vectors were then scaled to 0.01 Å before being added and subtracted from the CI structure. In the case of CASSCF, SF-TDDFT, and SI-SA-REKS, the crossing point was optimized at the respective level of theory. For SF-TDDFT, the CI optimization and branching plane vectors were obtained using Maeda's approach,[23] while for SI-SA-REKS the program CIOpt was used.[26] For the other cases (CASPT2 methods and XMCQDPT2), the CI points were not optimized but chosen as the nearest point to the crossing along the BLA scan. The solid and dashed black lines on the surfaces show the S_0 and S_1 energy profiles, respectively, along the DCV and passing through the CI.

a conical crossing. MS-CASPT2 and XMCQDPT2 allow coupling and therefore display the correct conical shape; the same is true for SF-TDDFT and SI-SA-REKS. In all of these cases, the CI's are sloped, consistent with the results of the BLA scans in Figures 3 and 4. In the case of SS-CASPT2(IPEA=0.25), MS-CASPT2(IPEA=0.25), and XMCQDPT2, the crossing points do not appear at the center of the plot simply because the CI was not optimized at the respective level of theory but rather was obtained at a crossing point along the BLA. Finally, the SS-CASPT2(IPEA=0) and MS-CASPT2(IPEA=0) curves display significant artifacts similar to those observed in the loops, due to their proximity to the CASSCF CI.[29,41]

Consequences for Semiclassical Molecular Dynamics. The ability of a method to correctly describe the branching plane in the proximity of a crossing may be essential for mechanistic studies or, even more, semiclassical dynamics studies. More specifically, semiclassical dynamics may be sensitive to the shape and topology of the intersection region, since the fate of a trajectory may depend on the crossing topology (e.g., linear or conical) as well as on the geometry and electronic structure at the point of surface hop, as reported in recent studies.[69,94,95] In order to investigate how the differences of the potential energy surfaces at crossings impact the outcome of semiclassical dynamics, we computed a set of 100 semiclassical trajectories (representing a vibrational wavepacket released from the Franck−Condon region of the S_1 potential energy surface) at the CASSCF and SS-CASPT2(IPEA=0.25) levels of theory using a PSB3 derivative (*trans*-3-MePSB3; see Figure 6A, left) as a model system. This derivative features a methyl substituent at C3 and therefore represents a better model of the all-*trans*-rPSB chromophore of microbial rhodopsins which almost exclusively isomerize about the C13−C14 double bond (see Scheme 1A). The BLA scan of 3Me-PSB3 is shown in Figure 6B. The CASSCF and SS-CASPT2(IPEA=0.25) energy profiles are quite similar. We find that CASSCF has an intermediate crossing topography (i.e., between peaked and sloped) where an S_1 minimum is intersected by the S_0 state whereas the SS-CASPT2(IPEA=0.25) crossing has a slightly sloped topography. In order to test the dynamics of the decay in the region of the conical intersection seam, the *trans*-3-MePSB3 model has also been pretwisted 25° about the reactive double bond (see Figure 6A). Such pretwisting not only makes the model more similar to the corresponding moiety of protein-bound chromophores but also bypasses a region of the S_1 energy surface where the CASSCF and SS-CASPT2 energy surfaces have different shapes.[30] This is important because in the present context we want to focus exclusively on the effect of the different dimensionality of the crossing.

The results of the dynamics simulations are shown in Figure 6C,D. These figure panels display how the C2−C3 torsional deformation, described by the dihedral angle (α), evolves as a function of time. The small circles correspond to surface hop points. Remarkably, and in spite of the different CASSCF and SS-CASPT2 crossing topology described above (a conical and linear topology, respectively), the S_1 to S_0 evolution of the two trajectory ensembles appears to be quite similar. This is illustrated by the similar progression of the average α value (see black lines in Figure 6BC) along the S_1 state, the similar branched pattern of the trajectory density along the entire 200 fs simulation, and the similar distribution of the hop (mainly S_1 to S_0 decay) points. The analysis of the time evolution of other geometrical coordinates leads to the same conclusion. Most importantly, the branching toward the cis and trans isomers (associated with α values of ca. 0° and 180°, respectively)
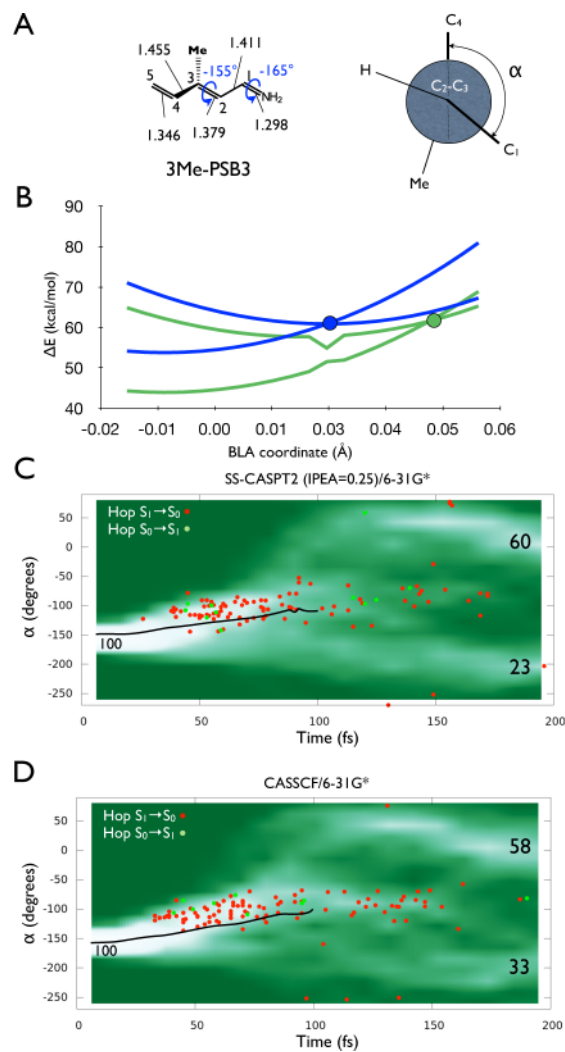

Figure 6. Comparison of the results of 100 CASSCF and 100 SS-CASPT2(IPEA=0.25) semiclassical trajectories. (A, left). The *trans*-3Me-PSB3 model used as a starting structure for thermal sampling which yielded 100 structures and velocities used to launch the semiclassical trajectories. The structure was optimized at the CASSCF level of theory with constraints on the C1−C2−C3−C4 and H−N−C1−C2 dihedrals shown in blue. These constraints were used to mimic pretwisting of the double bonds as in a protein environment and also to help overcome the locally excited region of the excited-state surface documented in ref 30. (A, right) Newman projection of 3Me-PSB3 showing the definition of the C1−C2−C3−C4 dihedral α. (B) CASSCF (blue) and SS-CASPT2(IPEA=0.25) (green) energy profiles along the BLA scan of 3Me-PSB3. This BLA scan was constructed in a way similar to the BLA scan in ref 29. (C and D) Change in α as a function of time for the 100 trajectories at the CASSCF and SS-CASPT2(IPEA=0.25) levels of theory, respectively. Rather than display 100 trajectories, we present the population density (in white, contrasted to a dark green background). The black line in each graph represents the average dihedral of all trajectories which are on the excited state at the given time, up to 100 fs. Red points represent hop events from S_1 to S_0, while green points represent back-hop events from S_0 to S_1. The numbers on the right side of the graph represent the number of trajectories which reached *cis*-3-MePSB3 after hopping (at around $\alpha = 0$) and the number of trajectories which reached *trans*-3-MePSB3 (at around $\alpha = -180°$).

occurring after the hop is also comparable. Indeed, at the CASSCF level, 58 trajectories photoisomerize to *cis*-3Me-PSB3 while 33 trajectories return to the *trans*-3Me-PSB3 and 9 trajectories remain unreacted on the excited state for the duration

of the 200 fs trajectory, whereas, at the SS-CASPT2 level, 60 trajectories photoisomerize, 23 decay back toward *trans*-3Me-PSB3, and 17 remain unreacted. A full analysis of these results, including the degree of uncertainty due to the fairly limited number of computed trajectories, is beyond the scope of the current study, whose main target is to asses the sensitivity of the PSB3 dynamics to its branching plane features. Here, we simply report that for selected pretwisted *trans*-3Me-PSB3 model and for the common initial conditions (which are generated at the HF level on the basis of the only CASSCF equilibrium structure; see Figure 6A) CASSCF and SS-CASPT2 yield qualitatively similar results. The generality of this statement as well as the reason for why it is true remain to be thoroughly investigated in future studies. In Figure 7 we only provide a tentative interpretation
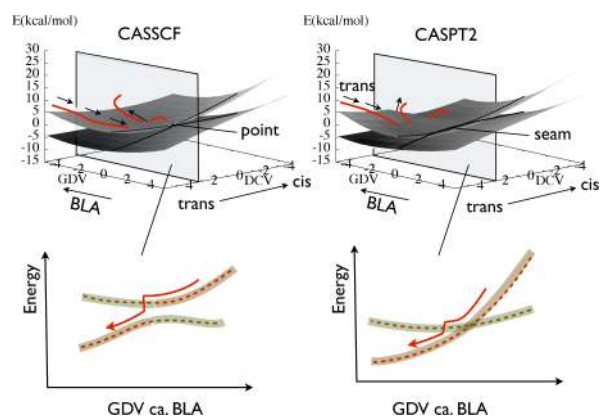
Figure 7. Scheme tentatively explaining why CASSCF and SS-CASPT2(IPEA=0.25) semiclassical dynamics may behave similarly despite the different topologies of the intersection and branching plane for the two methods. A typical trajectory in the case of 3Me-PSB3 oscillates along the BLA mode (which is roughly parallel to the GDV). As a result, the wave function along such a trajectory undergoes a large change in electronic structure whether it crosses an avoided crossing (as in the case of a CASSCF trajectory) or a linear crossing (as in the case of a SS-CASPT2 trajectory), and the molecule would have a large possibility of hopping in both cases (see bottom panels).

based on the fact that the geometrical deformation bringing about a sudden change in wave function character is BLA (see Figure 2A). For the system under investigation this is nearly parallel to the BP direction labeled GDV and nearly orthogonal to DCV. Since each trajectory will initially accelerate out of the Franck−Condon region along a double bond expansion/single bond contraction mode,[30,96,97] the CI region will be approached along a coordinate oscillating along BLA, as schematically illustrated in Figure 7. Here we need to stress, again, that the presented results are valid for the semiclassical dynamics scheme used in the calculation (e.g., quantum dynamics may yield a different picture), for the specific pretwisted system under investigation and for the selected set of 100 initial conditions. Different initial conditions, for instance obtained by sampling a less distorted chromophore (i.e., more distant from the CI points) and thus making more difficult and slower the evolution toward the CI region, may have resulted in different hop distributions and distinct dynamics for the two levels of theory. Further studies are clearly needed to address these issues in depth.

CONCLUSION

In the present work, we have presented a benchmarking protocol and used it to test the shape of the branching plane around

crossings located along the BLA path using several electronic structure methods. This benchmark may be used to distinguish between methods that produce a true (conical) crossing from methods that produce a linear crossing belonging to a $(3N − 7)$-dimensional IS. Note that the possibility of a CI belonging to a $(3N − 9)$-dimensional space cannot be probed by this protocol. The results expand our knowledge of the PSB3 potential energy surfaces obtained with different electronic structure methods and strengthen the use of PSB3 as a benchmark system for the development of reliable electronic structure methods. In particular, we have addressed the problem of obtaining the correct geometry, energy, shape, and dimensionality for CIs. The conclusions regarding the BP topology at different levels of theory are, likely, not limited to the CI of PSB3, but general. Using methods yielding a conical rather than a linear crossing in the BP may be essential for rigorous mechanistic or dynamics studies of processes driven by a surface crossing. Our study reveals that the choice of appropriate methods may be more limited than expected. However, preliminary tests reveal that semiclassical dynamics are qualitatively similar despite differences in the CI topology and BP, although this conclusion remains to be investigated more thoroughly in the future through further semiclassical dynamics and, possibly, quantum dynamics simulations.

ASSOCIATED CONTENT

S Supporting Information

Figure S1 showing the CASSCF, SS-CASPT2, MRCISD, MRCISD+Q, SI-SA-REKS/BH&HLYP, and SF-TDDFT/BH&HLYP conical intersection geometries used to construct the loops in Figures 3 and 4, Figure S2 showing the CASSCF and SI-SA-REKS branching plane vectors, Figures S3−S16 showing the S_0 and S_1 energies for each method along the loop as well as the charge-transfer character or coefficient of the closed-shell configuration of the ground state (only when available), and Figure 17 showing a superposition of the SF-TDDFT/BH&HLYP, SI-SA-REKS/BH&HLYP, and MS-CASPT2 minimum energy CI, and tables listing coordinates of the crossings used at the center of the loops and the CASSCF DCV and GDV and MECI, DCV, and GDV computed at the SI-SA-REKS/BH&HLYP and SF-TDDFT/BH&HLYP levels. This material is available free of charge via the Internet at http://pubs.acs.org.

AUTHOR INFORMATION

Corresponding Author

*E-mail: molivuc@bgnet.bgsu.edu, olivucci@unisi.it.

Notes

The authors declare no competing financial interest.

ACKNOWLEDGMENTS

3082

dx.doi.org/10.1021/ct500154k | *J. Chem. Theory Comput.* 2014, 10, 3074−3084

■ REFERENCES

(1) Teller, E. J. *J. Phys. Chem.* **1937**, *41*, 109−16.

(2) Herzberg, G.; Longuet-Higgins, H. C. *Discuss. Faraday Soc.* **1963**, *35*, 77−82.

(3) Zimmerman, H. E. *J. Am. Chem. Soc.* **1966**, *88*, 1564−5.

(4) Bonačić-Koutecký, V.; Koutecký, J.; Michl, J. *Angew. Chem., Int. Ed. Engl.* **1987**, *26*, 170−89.

(5) Klessinger, M.; Michl, J. *Excited states and photochemistry of organic molecules*; VCH: New York, 1995

(6) Bernardi, F.; Olivucci, M.; Robb, M. A. *Chem. Soc. Rev.* **1996**, *25*, 321−8.

(7) Schapiro, I.; Melaccio, F.; Laricheva, E. N.; Olivucci, M. *Photochem. Photobiol. Sci.* **2011**, *10*, 867−86.

(8) Domcke, W.; Yarkony, D. R. *Annu. Rev. Phys. Chem.* **2012**, *63*, 325−52.

(9) Mckinlay, R. G.; Źurek, J. M.; Paterson, M. J. *Adv. Inorg. Chem.* **2010**, *62*, 351−90.

(10) Sinicropi, A.; Andruniow, T.; De Vico, L.; Ferré, N.; Olivucci, M. *Pure. Appl. Chem.* **2005**, *77*, 977−93.

(11) Schapiro, I.; Ryazantsev, M. N.; Ding, W. J.; Huntress, M. M.; Melaccio, F.; Andruniow, T.; Olivucci, M. *Aust. J. Chem.* **2010**, *63*, 413−29.

(12) Matsika, S.; Krause, P. *Annu. Rev. Phys. Chem.* **2011**, *62*, 621−43.

(13) Garavelli, M.; Vreven, T.; Celani, P.; Bernardi, F.; Robb, M. A.; Olivucci, M. *J. Am. Chem. Soc.* **1998**, *120*, 1285−8.

(14) Levine, B. G.; Martínez, T. J. *Annu. Rev. Phys. Chem.* **2007**, *58*, 613−34.

(15) Frutos, L. M.; Andruniów, T.; Santoro, F.; Ferré, N.; Olivucci, M. *Proc. Natl. Acad. Sci. U. S. A.* **2007**, *104*, 7764−9.

(16) Hayashi, S.; Tajkhorshid, E.; Schulten, K. *Biophys. J.* **2009**, *96*, 403−16.

(17) Polli, D.; Altoè, P.; Weingart, O.; Spillane, K. M.; Manzoni, C.; Brida, D.; Tomasello, G.; Orlandi, G.; Kukura, P.; Mathies, R. A.; Garavelli, M.; Cerullo, G. *Nature* **2010**, *467*, 440−3.

(18) Yarkony, D. R. *Chem. Rev.* **2012**, *112*, 481−98.

(19) Atchity, G. J.; Xantheas, S. S.; Ruedenberg, K. *J. Chem. Phys.* **1991**, *95*, 1862.

(20) Ragazos, I. N.; Robb, M. A.; Bernardi, F.; Olivucci, M. *Chem. Phys. Lett.* **1992**, *197*, 217−23.

(21) Bearpark, M. J.; Robb, M. A.; Bernhard Schlegel, H. *Chem. Phys. Lett.* **1994**, *223*, 269−74.

(22) Yarkony, D. R. *J. Phys. Chem. A* **2004**, *108*, 3200−5.

(23) Maeda, S.; Ohno, K.; Morokuma, K. *J. Chem. Theory Comput.* **2010**, *6*, 1538−45.

(24) Koga, N.; Morokuma, K. *Chem. Phys. Lett.* **1985**, *119*, 371−4.

(25) Levine, B. G.; Ko, C.; Quenneville, J.; MartÍnez, T. J. *Mol. Phys.* **2006**, *104*, 1039−51.

(26) Levine, B. G.; Coe, J. D.; Martínez, T. J. *J. Phys. Chem. B* **2008**, *112*, 405−13.

(27) Granovsky, A. A. *Firefly*, Version 8.0.0; 2013; http://classic.chem.msu.su/gran/firefly/index.html.

(28) Epifanovsky, E.; Krylov, A. I. *Mol. Phys.* **2007**, *105*, 2515−25.

(29) Gozem, S.; Huntress, M.; Schapiro, I.; Lindh, R.; Granovsky, A. A.; Angeli, C.; Olivucci, M. *J. Chem. Theory Comput.* **2012**, *8*, 4069−80.

(30) Gozem, S.; Melaccio, F.; Lindh; Krylov, A. I.; Granovsky, A. A.; Angeli, C.; Olivucci, M. *J. Chem. Theory Comput.* **2013**, *9*, 4495−506.

(31) Gozem, S.; Schapiro, I.; Ferré, N.; Olivucci, M. *Science* **2012**, *337*, 1225−8.

(32) Yarkony, D. R. *Rev. Mod. Phys.* **1996**, *68*, 985.

(33) Gozem, S.; Krylov, A. I.; Olivucci, M. *J. Chem. Theory Comput.* **2013**, *9*, 284−92.

(34) Xu, X.; Gozem, S.; Olivucci, M.; Truhlar, D. G. *J. Phys. Chem. Lett.* **2013**, *4*, 253−8.

(35) Huix-Rotllant, M.; Filatov, M.; Gozem, S.; Schapiro, I.; Olivucci, M.; Ferre, N. *J. Chem. Theory Comput.* **2013**, *9*, 3917−32.

(36) Schapiro, I.; Neese, F. *Comput. Theor. Chem.* **2014**, DOI: 10.1016/j.comptc.2014.04.002.

(37) von Neumann, J.; Wigner, E. *Phys. Z.* **1929**, *30*, 467−70.

(38) Hättig, C. *Adv. Quantum Chem.* **2005**, *50*, 37−60.

(39) Köhn, A.; Tajti, A. *J. Chem. Phys.* **2007**, *127*, 044105.

(40) Andersson, K.; Malmqvist, P.; Roos, B. O. *J. Chem. Phys.* **1992**, *96*, 1218.

(41) Granovsky, A. A. *J. Chem. Phys.* **2011**, *134*, 214113.

(42) Angeli, C.; Cimiraglia, R.; Evangelisti, S.; Leininger, T.; Malrieu, J. P. *J. Chem. Phys.* **2001**, *114*, 10252.

(43) Angeli, C.; Pastore, M.; Cimiraglia, R. *Theor. Chem. Acc.* **2007**, *117*, 743−54.

(44) Krylov, A. I. *Chem. Phys. Lett.* **2001**, *338*, 375−84.

(45) Slipchenko, L. V.; Krylov, A. I. *J. Chem. Phys.* **2002**, *117*, 4694.

(46) Levchenko, S. V.; Krylov, A. I. *J. Chem. Phys.* **2004**, *120*, 175−85.

(47) Krylov, A. I. *Acc. Chem. Res.* **2006**, *39*, 83−91.

(48) Manohar, P. U.; Krylov, A. I. *J. Chem. Phys.* **2008**, *129*, 194105.

(49) Schwabe, T.; Grimme, S. *Phys. Chem. Chem. Phys.* **2006**, *8*, 4398−401.

(50) Grimme, S.; Neese, F. *J. Chem. Phys.* **2007**, *127*, 154116.

(51) Schwabe, T.; Grimme, S. *Phys. Chem. Chem. Phys.* **2007**, *9*, 3397−406.

(52) Lee, C.; Yang, W.; Parr, R. G. *Phys. Rev. B: Condens. Matter Mater Phys.* **1988**, *37*, 785−9.

(53) Shao, Y.; Head-Gordon, M.; Krylov, A. I. *J. Chem. Phys.* **2003**, *118*, 4807.

(54) Bonačić-Koutecký, V.; Schöffel, K.; Michl, J. *Theor. Chem. Acc.* **1987**, *72*, 459−74.

(55) Finley, J.; Malmqvist, P.; Roos, B. O.; Serrano-Andrés, L. *Chem. Phys. Lett.* **1998**, *288*, 299−306.

(56) Ghigo, G.; Roos, B. O.; Malmqvist, P. K. *Chem. Phys. Lett.* **2004**, *396*, 142−9.

(57) Langhoff, S. R.; Davidson, E. R. *Int. J. Quantum Chem.* **1974**, *8*, 61−72.

(58) Werner, H. J.; Kállay, M.; Gauss, J. *J. Chem. Phys.* **2008**, *128*, 034305.

(59) Hirata, S.; Head-Gordon, M. *Chem. Phys. Lett.* **1999**, *314*, 291−9.

(60) Filatov, M.; Shaik, S. *Chem. Phys. Lett.* **1999**, *304*, 429−37.

(61) Kazaryan, A.; Heuver, J.; Filatov, M. *J. Phys. Chem. A* **2008**, *112*, 12980−8.

(62) Filatov, M. *J. Chem. Theory Comput.* **2013**, *9*, 4526−41.

(63) Li, S. L.; Marenich, A. V.; Xu, X.; Truhlar, D. G. *J. Phys. Chem. Lett.* **2014**, *5*, 322−8.

(64) Wang, F.; Ziegler, T. *J. Chem. Phys.* **2004**, *121*, 12191.

(65) Yamaguchi, K.; Takahara, Y.; Fueno, T. In *Applied. Quantum. Chemistry*; Smith, V. H., Schaefer, H. F., Morokuma, K., Eds.; D. Reidel: Dordrecht, The Netherlands, 1986; pp 155−184.

(66) Shoji, M.; Koizumi, K.; Kitagawa, Y.; Kawakami, T.; Yamanaka, S.; Okumura, M.; Yamaguchi, K. *Chem. Phys. Lett.* **2006**, *432*, 343−7.

(67) Hase, W. L.; Duchovic, R. J.; Hu, X.; Komornicki, A.; Lim, K. F.; Lu, D.-H.; Peslherbe, G. H.; Swamy, K. N.; Van de Linde, S. R.; Varandas, A. J. C. *QCPE Bull.* **1996**, *16*, 43.

(68) Aquilante, F.; De Vico, L.; Ferré, N.; Ghigo, G.; Malmqvist, P. A.; Neogrády, P.; Pedersen, T. B.; Pitoňák, M.; Reiher, M.; Roos, B. O.; Serrano-Andrés, L.; Urban, M.; Veryazov, V.; Lindh, R. *J. Comput. Chem.* **2010**, *31*, 224−47.

(69) Schapiro, I.; Ryazantsev, M. N.; Frutos, L. M.; Ferré, N.; Lindh, R.; Olivucci, M. *J. Am. Chem. Soc.* **2011**, *133*, 3354−64.

(70) Swope, W. C.; Andersen, H. C.; Berens, P. H.; Wilson, K. R. *J. Chem. Phys.* **1982**, *76*, 637.

(71) Tully, J. C. *J. Chem. Phys.* **1990**, *93*, 1061.

(72) Hammes-Schiffer, S.; Tully, J. C. *J. Chem. Phys.* **1994**, *101*, 4657.

(73) Granucci, G.; Persico, M. *J. Chem. Phys.* **2007**, *126*, 134114.

(74) Frisch, M. J.; Trucks, G. W.; Schlegel, H. B.; Scuseria, G. E.; Robb, M. A.; Cheeseman, J. R.; Montgomery, J. A.; Vreven, T.; Kudin, K. N.; Burant, J. C.; Millam, J. M.; Iyengar, S. S.; Tomasi, J.; Barone, V.; Mennucci, B.; Cossi, M.; Scalmani, G.; Rega, N.; Petersson, G. A.; Nakatsuji, H.; Hada, M.; Ehara, M.; Toyota, K.; Fukuda, R.; Hasegawa, J.; Ishida, M.; Nakajima, T.; Honda, Y.; Kitao, O.; Nakai, H.; Klene, M.; Li, X.; Knox, J. E.; Hratchian, H. P.; Cross, J. B.; Bakken, V.; Adamo, C.; Jaramillo, J.; Gomperts, R.; Stratmann, R. E.; Yazyev, O.; Austin, A. J.; Cammi, R.; Pomelli, C.; Ochterski, J. W.; Ayala, P. Y.; Morokuma, K.; Voth, G. A.; Salvador, P.; Dannenberg, J. J.; Zakrzewski, V. G.; Dapprich, S.; Daniels, A. D.; Strain, M. C.; Farkas, O.; Malick, D. K.; Rabuck, A. D.; Raghavachari, K.; Foresman, J. B.; Ortiz, J. V.; Cui, Q.; Baboul, A. G.; Clifford, S.; Cioslowski, J.; Stefanov, B. B.; Liu, G.; Liashenko, A.; Piskorz, P.; Komaromi, I.; Martin, R. L.; Fox, D. J.; Keith, T.; Laham, A.; Peng, C. Y.; Nanayakkara, A.; Challacombe, M.; Gill, P. M. W.; Johnson, B.; Chen, W.; Wong, M. W.; Gonzalez, C.; Pople, J. A. *Gaussian 03*, Revision C.02; Gaussian: Wallingford, CT, USA, 2004.

(75) Werner, H. J.; Knowles, P. J.; Knizia, G.; Manby, F. R.; Schütz, M.; Celani, P.; Korona, T.; Lindh, R.; Mitrushenkov, A.; Rauhut, G.; Shamasundar, K. R.; Adler, T. B.; Amos, R. D.; Bernhardsson, A.; Berning, A.; Cooper, D. L.; Deegan, M. J. O.; Dobbyn, A. J.; Eckert, F.; Goll, E.; Hampel, C.; Hesselmann, A.; Hetzer, G.; Hrenar, T.; Jansen, G.; Köppl, C.; Liu, Y.; Lloyd, A. W.; Mata, R. A.; May, A. J.; McNicholas, S. J.; Meyer, W.; Mura, M. E.; Nicklass, A.; O'Neill, D. P.; Palmieri, P.; Pflüger, K.; Pitzer, R.; Reiher, M.; Shiozaki, T.; Stoll, H.; Stone, A. J.; Tarroni, R.; Thorsteinsson, T.; Wang, M.; Wolf, A. *MOLPRO*, version 2010.1, a package of ab initio programs; University College Cardiff Consultants: Cardiff, U.K., 2010.

(76) Schmidt, M. W.; Baldridge, K. K.; Boatz, J. A.; Elbert, S. T.; Gordon, M. S.; Jensen, J. H.; Koseki, S.; Matsunaga, N.; Nguyen, K. A.; Su, S. *J. Comput. Chem.* **1993**, *14*, 1347−63.

(77) Shao, Y.; Molnar, L. F.; Jung, Y.; Kussmann, J.; Ochsenfeld, C.; Brown, S. T.; Gilbert, A. T. B.; Slipchenko, L. V.; Levchenko, S. V.; O'Neill, D. P.; DiStasio, R. A.; Lochan, R. C.; Wang, T.; Beran, G. J. O.; Besley, N. A.; Herbert, J. M.; Lin, C. Y.; Van Voorhis, T.; Chien, S. H.; Sodt, A.; Steele, R. P.; Rassolov, V. A.; Maslen, P. E.; Korambath, P. P.; Adamson, R. D.; Austin, B.; Baker, J.; Byrd, E. F. C.; Dachsel, H.; Doerksen, R. J.; Dreuw, A.; Dunietz, B. D.; Dutoi, A. D.; Furlani, T. R.; Gwaltney, S. R.; Heyden, A.; Hirata, S.; Hsu, C. -P. P.; Kedziora, G.; Khalliulin, R. Z.; Klunzinger, P.; Lee, A. M.; Lee, M. S.; Liang, W.; Lotan, I.; Nair, N.; Peters, B.; Proynov, E. I.; Pieniazek, P. A.; Rhee, Y. M.; Ritchie, J.; Rosta, E.; Sherrill, C. D.; Simonett, A. C.; Subotnik, J. E.; Woodcock, H. L.; Zhang, W.; Bell, A. T.; Chakraborty, A. K.; Chipman, D. M.; Keil, F. J.; Warshel, A.; Hehre, W. J.; Schaefer, H. F.; Kong, J.; Krylov, A. I.; Gill, P. M. W.; Head-Gordon, M. *Phys. Chem. Chem. Phys.* **2006**, *8*, 3172−91.

(78) Neese, F. *ORCA*, version 2.9.1; Max-Planck-Institut für Chemische Energiekonversion: Muheim an der Ruhr, Germany, 2004.

(79) Kraka, E.; Filatov, M.; Zou, W.; Grafenstein, J.; Izotov, D.; Gauss, J.; He, Y.; Wu, A.; Polo, V.; Olsson, L.; Konkoli, Z.; He, Z.; Cremer, D. COLOGNE2012; Southern Methodist University: Dallas, TX, 2012.

(80) Olkhov, R. V.; Bally, T. *MOplot*, v.1.86; http://www-chem.unifr.ch/tb/moplot/moplot.html.

(81) Matsika, S. *Chem. Phys.* **2008**, *349*, 356−62.

(82) Malrieu, J.-P.; Heully, J.-L.; Zaitsevskii, A. *Theor. Chim. Acta* **1995**, *90*, 167−87.

(83) Zaitsevskii, A.; Malrieu, J.-P. *Chem. Phys. Lett.* **1995**, *233*, 597−604.

(84) Rozgonyi, T.; Gonzalez, L. *J. Phys. Chem. A* **2006**, *110*, 10251−9.

(85) Shiozaki, T.; Gyorffy, W.; Celani, P.; Werner, H. J. *J. Chem. Phys.* **2011**, *135*, 081106.

(86) Serrano-Andrés, L.; Merchán, M.; Lindh, R. *J. Chem. Phys.* **2005**, *122*, 104107.

(87) Send, R.; Furche, F. *J. Chem. Phys.* **2010**, *132*, 044107.

(88) Keal, T. W.; Wanko, M.; Thiel, W. *Theor. Chem. Acc.* **2009**, *123*, 145−56.

(89) Isegawa, M.; Truhlar, D. G. *J. Chem. Phys.* **2013**, *138*, 134111.

(90) Minezawa, N.; Gordon, M. S. *J. Phys. Chem. A* **2011**, *115*, 7901−11.

(91) Huix-Rotllant, M.; Natarajan, B.; Ipatov, A.; Wawire, C. M.; Deutsch, T.; Casida, M. E. *Phys. Chem. Chem. Phys.* **2010**, *12*, 12811−25.

(92) Sears, J. S.; Sherrill, C. D.; Krylov, A. I. *J. Chem. Phys.* **2003**, *118*, 9084−94.

(93) Rinkevicius, Z.; Vahtras, O.; Ågren, H. *J. Chem. Phys.* **2010**, *133*, 114104.

(94) Weingart, O. *Chem. Phys.* **2008**, *349*, 348−55.

(95) Weingart, O.; Altoè, P.; Stenta, M.; Bottoni, A.; Orlandi, G.; Garavelli, M. *Phys. Chem. Chem. Phys.* **2011**, *13*, 3645−8.

(96) Migani, A.; Robb, M. A.; Olivucci, M. *J. Am. Chem. Soc.* **2003**, *125*, 2804−8.

(97) González-Luque, R.; Garavelli, M.; Bernardi, F.; Merchán, M.; Robb, M. A.; Olivucci, M. *Proc. Natl. Acad. Sci. U. S. A.* **2000**, *97*, 9379−84.